We are IntechOpen,
the world's leading publisher of
Open Access books
Built by scientists, for scientists

4,800
Open access books available

122,000
International authors and editors

135M
Downloads

Our authors are among the

154
Countries delivered to

TOP 1%
most cited scientists

12.2%
Contributors from top 500 universities

BOOK
CITATION
INDEX
CLARIVATE ANALYTICS
INDEXED

WEB OF SCIENCE™

Selection of our books indexed in the Book Citation Index
in Web of Science™ Core Collection (BKCI)

Interested in publishing with us?
Contact book.department@intechopen.com

Numbers displayed above are based on latest data collected.
For more information visit www.intechopen.com

Phonon Confinement Effect in III-V Nanowires

Begum N[1], Bhatti A S[1], Jabeen F[2], Rubini S[2], Martelli F[2]

[1]Department of Physics, COMSATS Institution of Information Technology, Islamabad,
[2]Laboratorio Nazionale TASC INFM-CNR, S.S. 14, km 163,5, 34012 Trieste,
[1]Pakistan
[2]Italy

1. Introduction

Novel properties offered by self assembled nanowires (NWs) based on III-V materials, make them a potential candidate for electronic and optoelectronic industry. An emerging field, "spintronic" is of marvellous importance in scientific and technological applications. Dilute magnetic semiconductors (DMS) specially the discovery of Mn doped III-As [1,2] leads the way to fabrication of semiconductor spin devices[3].

A wide number of III-V NWs have been grown by several techniques, including, metal-organic vapor phase epitaxy [8, 9] and molecular beam epitaxy (MBE) [10]. One major problem of self assembled nanowires is the presence of defects in these NWs.

Work has been reported on the analysis of defects and disorders in heterostructures, thin films and in crystals by using the phonon confinement model [11-13]. All these authors gave the qualitative analysis of defects and disorders in thin films or single crystals but to the best of our knowledge no one has estimated the defect density in a single NW.

Here, we study the structural defects present along the body of NWs carried out by means of μ-Raman scattering. A detailed analysis of the defect density in GaAs and InAs NWs and surface phonons will be presented. Phonon confinement model (PCM) will be used to fit the LO phonon peaks, which also takes into account contribution for asymmetry in the line shape due to presence of surface optical (SO) phonons and structural defects. This also allows us to determine the correlation lengths in these wires, the average distance between defects and defect density in these nanowires. Influence of these defects on SO phonon will also be investigated. Behavior of SO phonon modes by using the model presented by Ruppin and Englman will be discussed in detail.

2. Raman spectroscopy

A typical micro-Raman system consists of a microscope, excitation laser, filters, slits, diffraction grating, necessary optics, detector and post-processing software. Selection of appropriate light source for micro-Raman spectroscopy is of great importance because the Raman scattered photon have frequencies shift relative to the excitation frequencies. Raman signals are usually much weaker than the excitation intensity. For strong scattering material only one Raman scattered photon can be explored for every 10^7 incident photons. For the purpose coherent light source (laser) is preferred due to its high power, monochromatic and

collimated beam nature. Laser light after entering the system is governed by neutral density (ND) filters. After passing through the spatial filter, which removes the higher order spatial modes so that the beam achieves a better focus, the light is directed to the microscope to focus on the sample. Scattered light from the sample is then collected by the objective and directed to the spectrometer. On its return path elastically scattered light is filtered by the holographic filter. Raman light is then separated by the diffraction grating into discrete wavelengths, where each frequency is measured simultaneously. Final Raman signal is then directed to the CCD detector. Assuming a static scan is made, only a finite range of wavelengths reach the CCD via the diffraction grating. Photoelectrons are created in the CCD upon exposure to the scattered beam. The dispersed beam is spread vertically across horizontal lines of pixels, which are binned, or summed, to integrate each signal. This electric signal is then processed by the integrated system software.
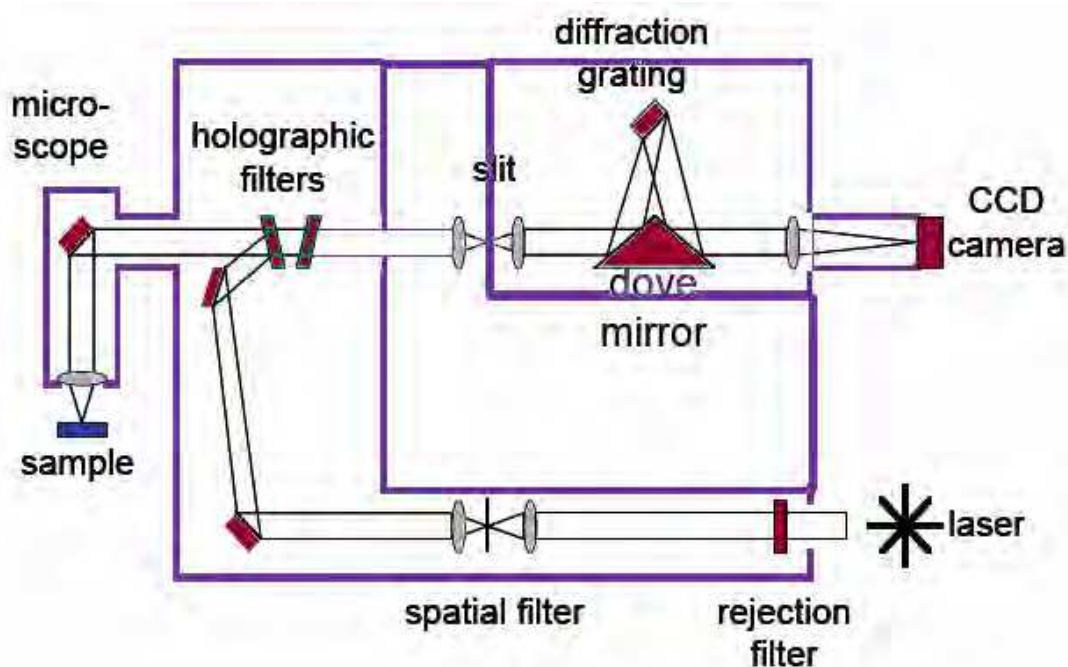

Fig. 1. Schematic of micro-Raman spectrometer. Where a collimated monochromatic light beam is focused on the sample and scattered light is directed through the optics of spectrometer and measured by CCD detector.

In the present case Raman spectra from the GaAs and InAs NWs grown on different substrates (SiO_2, GaAs (001) and GaAs (111)B substrates) with different catalysts (Au, Mn) by using MBE growth technique, were recorded at room temperature by using the Renishaw 1000 micro-Raman system equipped with CCD detector in pure backscattering geometry, with the wires lying in the plane of incidence of the incoming light. The excitation source was 514.5 nm line of an Ar^+ ion laser with a spot diameter of about 400 nm and excitation density of 1.67 mW/μm^2 for GaAs NWs and 0.56 mW/μm^2 for InAs NWs. Other details of NWs growth and Raman experimentation can be found in reference [7, 18- 21]. In order to measure the light scattered by single nanowires, after the growth, the wires were mechanically transferred onto a Si substrate. All the data presented here was obtained from single nanowire scattering. To achieve a statistically significance into the NW quality Raman spectra were taken on hundreds of wires.

3. Growth of the nanowires

GaAs and InAs NWs were synthesized by means of solid source molecular beam epitaxy at different growth temperatures ((540-620) °C for Mn-assisted GaAs NWs; (580-620) °C for Au-assisted GaAs NWs, and (390–430) °C for InAs NWs independently of the catalyst used) on SiO_2, ox-GaAs (100), and GaAs(111)B substrates. For the growth of NWs 1 nm of Mn or Au-catalyst was used. High density of NWs has been obtained on SiO_2 for either Au or Mn-catalyzed GaAs NWs (Figure 2 (a) & (b)). NW length was found as high as $20\,\mu m$ with the diameter in the range from few tens to about 200 nm. GaAs (100) and GaAs (111)B substrate gives the oriented NWs, which are much shorter than the NWs grown on SiO_2 (Figure 2 (c) & (d)). Figure 2(e) and 2(f) show the InAs NWs obtained on SiO_2 with the use of Au or Mn as catalyst, respectively.
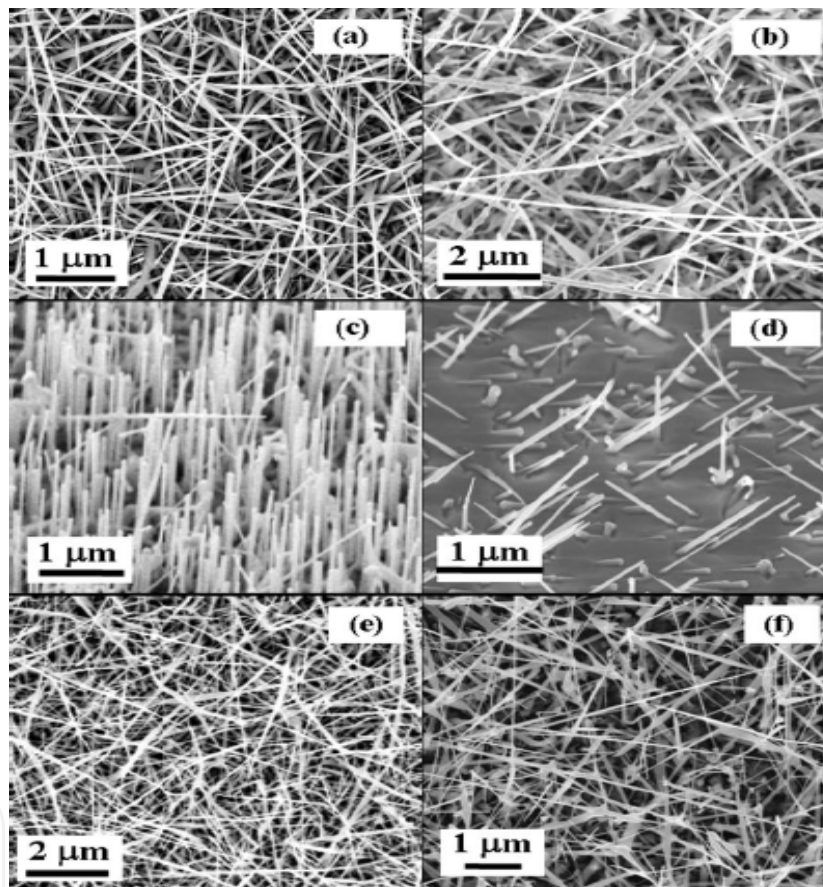

Fig. 2. SEM images of Au- and Mn-catalyzed NWs grown on different substrates: (a) Au-catalyzed GaAs NWs grown on SiO_2 substrate, (b) Mn-catalyzed GaAs NWs grown on SiO_2 substrate, (c) Au-catalyzed GaAs NWs grown on GaAs (111) *B*, (d) Au-catalyzed GaAs NWs grown on GaAs (100) substrate, (e) Au-catalyzed InAs NWs grown on SiO_2 substrate, and (f) Mn-catalyzed InAs on SiO_2. All images are plan views except (c) and (d), which were taken with the sample tilted by 45°.

4. Raman line shape analysis of GaAs and InAs semiconductor NWs

Raman spectra provide not only the basic structural information about the structure under investigation but also subtle spectra alterations can be used to access the nano-scale

structural changes. In III-V and other crystals with zincblende structure, the long range Coulomb forces split the LO and TO phonons at small k [22]. according to Raman selection rules only LO phonon can be observed in the backscattering geometry from <100> surface. But defects and electric field affects the scattering efficiency and the line shape of LO phonons. Therefore the line shape and FWHM of Raman mode provide useful information about the quality of semiconductor nanostructures. TO phonon scattering is forbidden in the backscattering geometry. However, structural disorder, alloy disorder and impurities can break the selection rule and activate the TO phonon. A Raman spectrum is therefore, a unique tool for probing the structural defects in nanostructures. In nanostructures the Raman spectrum remains sufficiently similar to that of the corresponding bulk material to facilitate the direct identification of the material. Once the Raman spectra are known, structural defects can be characterized through the mode variation [11, 23]. Besides, the observation of any theoretically forbidden mode is a very sensitive probe of lattice distortions.
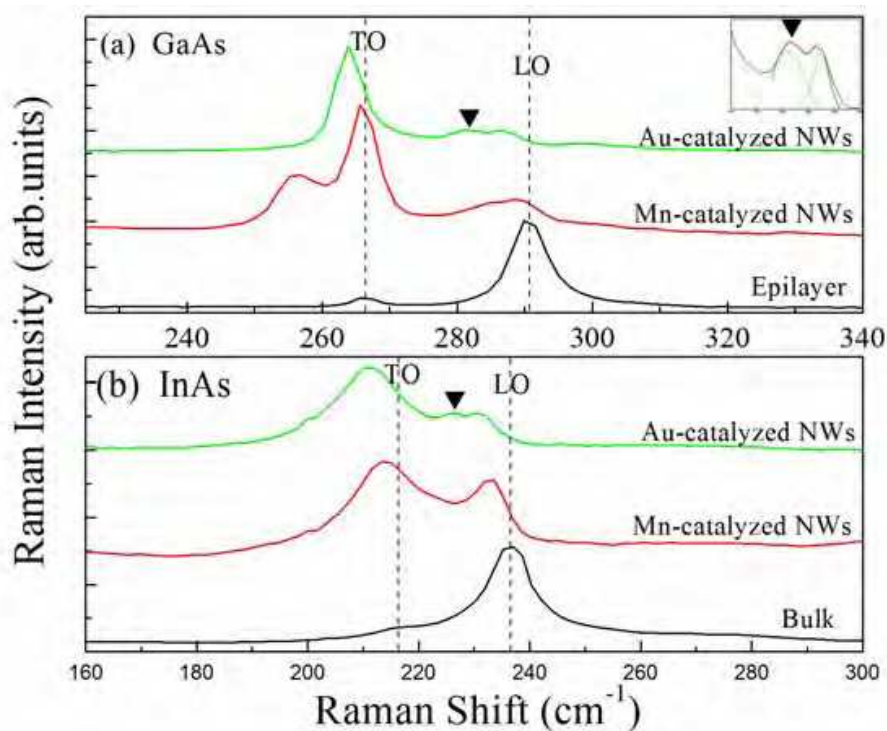

Fig. 3. Raman spectra of (a) GaAs and (b) InAs NWs in comparison of their respective bulk spectra. Surface phonon mode activated in NWs is marked by solid triangle. Inset shows the clear splitting of LO phonon mode indicating the SO phonon by solid triangle. Green curves in inset indicate the lorentzian fitting [20].

Micro-Raman spectroscopy is particularly well suited to study the III-V semiconductor NWs, because it gives good signal of the 1st order Raman spectra for both LO and TO phonons of III-V semiconductor material. Figure 3 illustrate this fact, where the representative Raman spectra of (a) GaAs NWs and (b) InAs NWs grown with two different catalysts, Au-catalyzed NWs (top spectrum), Mn-catalyzed NWs (middle spectrum) and GaAs epilayers or InAs bulk (bottom-most spectrum) are shown [20]. Raman spectra shown in Figure 3 are for the NWs grown on SiO$_2$ substrate. Raman spectra of GaAs epilayers gives TO peak at ~266.15 cm^{-1} and LO peak at ~ 290.59 cm^{-1}, while InAs bulk gives TO peak at
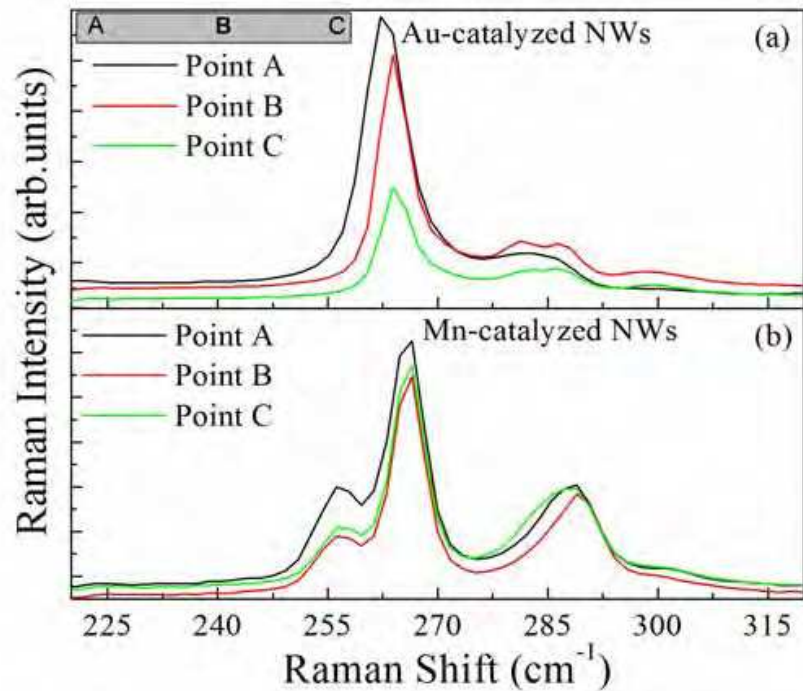
Fig. 4. Raman spectra taken at different points of single NW of (a) Au- and (b) Mn-catalyzed GaAs NWs. The inset schematically shows the single NW indicating the points where Raman spectra are taken.
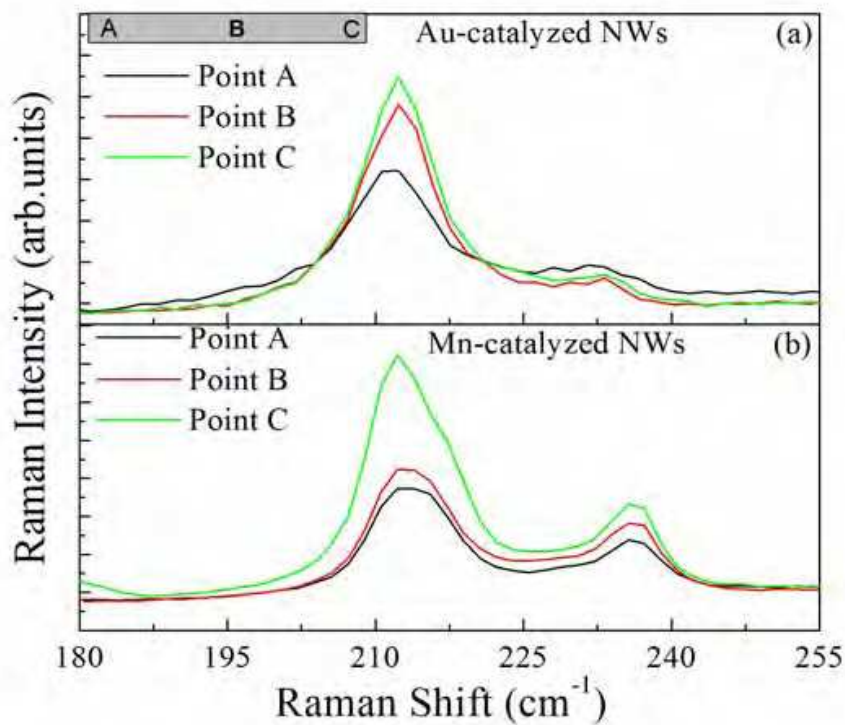

Fig. 5. Raman spectra taken at different points of single NW of (a) Au- and (b) Mn-catalyzed InAs NWs. The inset schematically shows the single NW indicating the points where Raman spectra are taken.

~217.14 cm^{-1} and LO peak at ~ 237.50 cm^{-1}. Raman spectrum of NWs shows that both TO and LO peaks are shifted toward lower energy with asymmetrical broadening. There is another peak observed between LO and TO phonon peak marked by inverted solid triangle in the Figure 3 (a) & (b), which can be related to the surface optical phonon (SO). Inset shows the clear splitting of LO phonon mode indicating the SO phonon by solid triangle. Solid black lines in the inset are the experimentally recorded data while green lines are results from a multiple Lorentzian fit. This peak is not resolvable in all the cases. Where this peak is not resolvable, LO peak shows more broadening and asymmetry due to weak contribution from the SO phonon. In those cases where this peak was not resolvable multiple Lorentzian fitting was done to resolve the LO peak in two peaks for having the contribution of SO phonons in LO peak. LO phonon lines were fitted with PCM to determine the correlation length, which also include SO phonon contribution. A detailed analysis of SO phonons and the influence of defects (in terms of correlation length) on SO phonons will be discussed later in this paper. In case of GaAs NWs there is another peak observed at ~ 255 cm^{-1} on low energy side of TO phonon.

The downshift in Raman lines observed in the wires is always larger for the LO phonon than for the TO phonon at low excitation intensities. The downshift with respect to epilayer shows variation from wire to wire and even within single nanowire. Figure 4 shows the single NW Micro-Raman spectra taken along the axis of the NW for (a) Au-catalyzed and (b) Mn-catalyzed GaAs NWs. Inset shows the schematic of the NW indicating the points where spectra has been taken. The spectra confirm that downshift varies even within a single NW. It also shows that the peak at 255 cm^{-1} is not found in all GaAs NWs. Figure 5 shows the single NW Micro-Raman spectra for (a) Au and (b) Mn-catalyzed InAs NWs. As for the shift measured for the LO phonon, however, in all those cases where no SO line is clearly distinguishable, the real LO downshift is smaller by a few cm^{-1} because of the presence of SO contribution that could not be resolved. This is in particular important for all the largest values given. Within a single wire the variation in the LO energy downshift is in general smaller, varying less than a factor of 2, except for very few wires, where the measured variation is larger.

In all of the spectra we have observed that the TO phonon appears much more intense than the LO phonon, independently of the wire orientation with respect to the plane of measurement. The intensity ratio I_{TO}/I_{LO} for NWs was found to be much larger (>1.5) than the I_{TO}/I_{LO} ratio of the GaAs epilayers (< 0.1). Similar ratios have also been reported by other groups for III-V NWs [8, 24]. The I_{TO}/I_{LO} intensity ratio strongly depends on the crystal orientation, geometry of the measurement but also on the surface electric field [see, *e.g.*, 25]. Our wires have a wurtzite crystal lattice and grown in the (0001) direction [7, 26] with large surface-to-volume ratio. Therefore, surface electric field may play an important role in determining the TO and LO line intensity.

4.1 Factors affecting the downshift and asymmetrical broadening of LO and TO phonons

Peak shift (red shift or blue shift) and asymmetrical broadening of Raman line shape may lead to the important information related to the system under investigation. Many factors can be involved in this shift and broadening of the Raman line shape. Tensile and compressive stress causes the Raman band to red shift and blue shift, respectively. Disordered and low dimensional systems (nanowires and quantum dots) lead to the asymmetrical broadening and downshift of the one-phonon Raman band. But another

factor that results in downshift and asymmetrical broadening of 1st order Raman band is the thermal heating process, which results in softening of the lattice parameter with increasing temperature and leading to the fano line shape. Detailed studies of the temperature dependence of the first order Raman band have been reported by many authors [27].

Piscanec and co-workers pointed out for Si NWs [30], heating of the wires by the impinging light lead to a downshift of the phonon energy. Similar effect was observed in present case of III-V NWs. This is shown in Figure 6(a) where we depict two spectra taken on Au-catalysed GaAs wire at two different excitation intensities. Figure 6(b) and 6(c) shows the energy downshift as a function of the excitation intensity representative for GaAs and InAS NWs, respectively. A clear saturation is observed at low intensities and below $I_0/10$ (where I_0 is the incident laser intensity) no further reduction of the downshift is observed. This
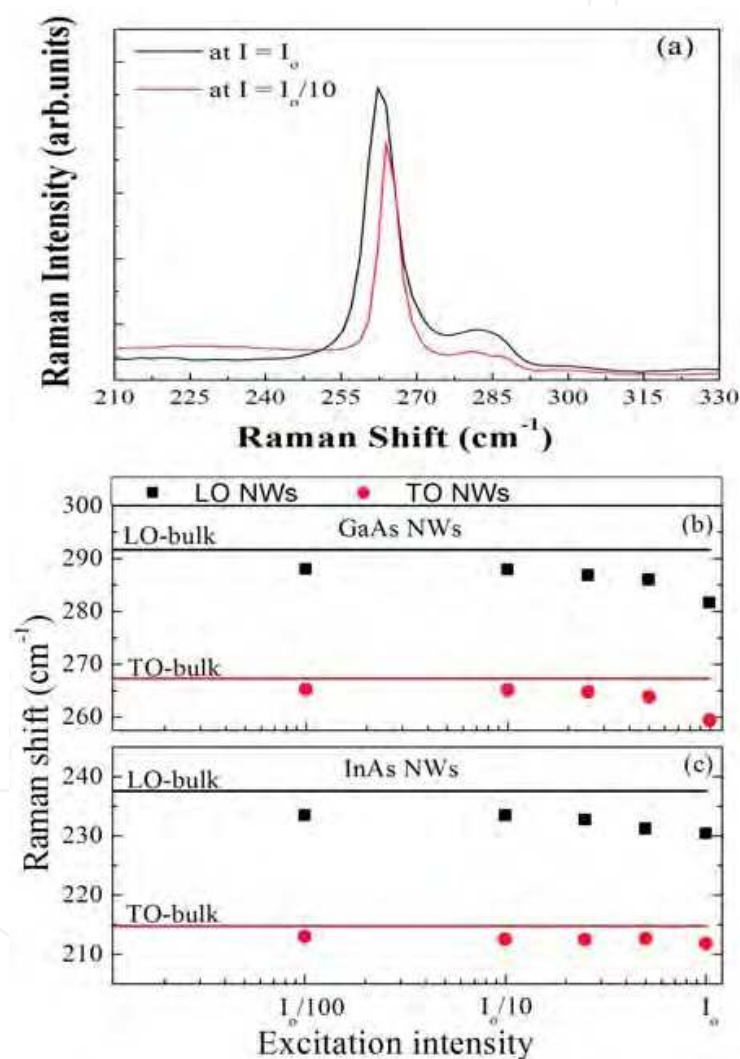

Fig. 6. (a) Raman spectra of an Au-catalyzed GaAs NW at different excitation intensities showing the TO peak shift due to heating effect: the red solid curve is taken with an excitation intensity ten times higher than the blue dotted curve. The red curve has been shifted upward for sake of clarity. (b) LO (black squares) and TO (red rhombuses) phonon line energies vs the excitation intensity. The data, given for a single wire, are representative of the general behavior. The black and red lines are the energy position of LO and TO phonons in the epitaxial GaAs. (c) The same as in (b) but for InAs.

behaviour has been observed to be quantitatively similar in all of the several wires investigated by μ-Raman belonging to both GaAs and InAs. Therefore, in order to avoid heating-induced downshift, all of the other data shown, analysed and discussed here have been recorded at excitation intensities that do not induce a measurable lattice heating in the wires. We notice that weaker light intensities are necessary to avoid heating for InAs NWs compared to GaAs NWs. This is easily explained by the fact that the band-gap of InAs is smaller than that of GaAs. The e-h pairs excited by the green light hence have a higher extra energy to be dissipated through the crystal lattice.

Small physical dimensions of the material may lead to a downshift and a broadening of the LO-Raman line because of the relaxation of the $q = 0$ selection rule. The size of our wires with diameter 20 nm to 200 nm, however, is too large to explain the observed downshift by the reduced size of the NWs. Calculations by Campbell and Fauchet [34] in the case of an infinitely long cylindrical microstructure showed that a diameter below 3 nm is required to downshift the LO feature by 4 cm^{-1}. The diameter of our NWs is 10 to 70 times larger, ruling out this type of explanation. As discussed below, we suggest that the relaxation of the $q = 0$ selection rule that can explain our data is due to the presence of lattice defects in the nanowires.

Downshift and broadening of the LO phonon line can be understood in the framework of the same "Phonon confinement model" proposed by Richter *et al.* [11] and by Tiong and coworkers [35] and generalized by Campbell and Fauchet [34] that has also been used to explain the size-induced energy downshift observed for very small NWs. This model was proposed to describe the crystalline quality by introducing a parameter known as correlation length, which is defined as the average size of the material homogeneity region. Correlation length may correspond to the actual grain size, average distance between defects, distribution of atoms in nominally disordered semiconducting alloys, and short range clustering in semiconducting alloys [11, 23, 36-37]. However, in our case the downshift of the Raman line gives account for the average size of defect-less regions, the smaller giving rise to larger downshifts.

The peak on low energy side of the TO phonons (at ~ 255cm^{-1}) can be assigned to the Raman scattering from the oxidized GaAs [38-39]. The assignment is also supported by the remark that this peak is observed with higher probability in Mn-catalyzed wires that show larger oxidized sidewalls than those catalyzed by Au [7].

5. Phonon confinement model (PCM)

One way to investigate the lattice disorders is the Raman line shape analysis using "the phonon confinement model (PCM)". This model describe the crystalline quality by the introduction of an important parameter known as "correlation length", defined as the average size of the material homogeneity region *i.e.,* the average distance between two defects [11].

Malayah *et al.* [23] study the misfit dislocation density near the interface in a GaAs/Si hetrostructure by using the Raman line-shape analysis. They calculate the broadening and frequency shift of the LO and TO phonons corresponding to the correlation length (the average distance between two defects) by using PCM as shown in Figure 7. By locating the experimental values of frequency shift corresponding value of the correlation length can easily be calculated. They also compare the values of the defect density calculated by the PCM with that of the found by TEM and prove that Raman spectroscopy is as good as that of TEM for finding the defect density in any structure.
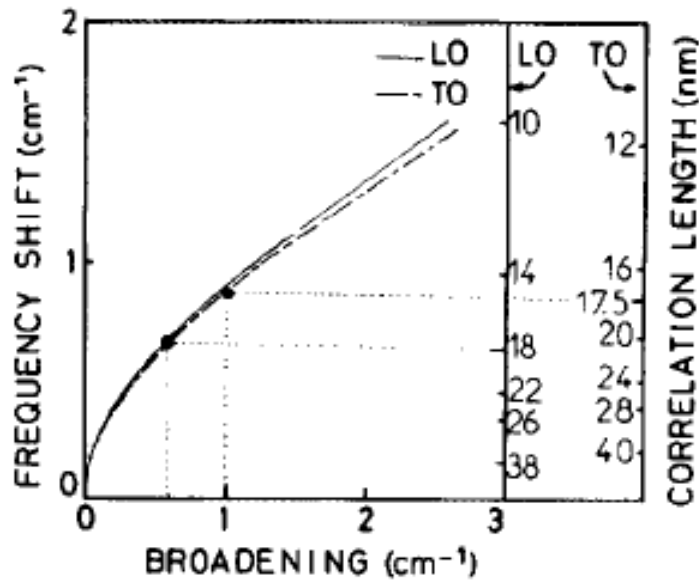
Fig. 7. Calculation performed using the PCM. The peak position shift and broadening scales are for both LO and TO modes. The dot refer to values of the broadening at the interface deduced from the fitting procedure [23].

The phonon confinement introduces additional contributions on the low frequency side of the single crystal phonon mode and resulting peak becomes asymmetric. Normally momentum conservation in single crystals allows only phonon modes with a wave vector $q \sim 0$ (close to the centre of the Brillouin zone). In phonon confinement model broadening is ascribed to the relaxation of the $q \sim 0$ selection rule in the small confinement region when vibrational modes away from the BZ centre contribute to the Raman scattering. The shift in LO peak energy is proportional to the phonon confinement region. Phonon can be confined by any "spatially limiting" feature in the confinement region (*e.g.,* twins, stacking faults, vacancies, boundaries, pores *etc*). According to the phonon confinement model (PCM), the Raman line intensity, I (ω) at the frequency ω can be written as [11]:

$$I(\omega) \cong \int_{BZ} \frac{|C(0,q)|^2 \, d^3 q}{\left(\omega - \omega(q)\right)^2 + \left(\dfrac{\Gamma_0}{2}\right)^2} , \qquad (1)$$

where $|C(0,q)|^2 = e^{-\frac{q^2 L^2}{16\pi^2}}$ is the Fourier coefficient, q is wave vector, L is the average distance between defects, Γ_0 is the natural line width (FWHM) and $\omega(q)$ is LO phonon dispersion. For the LO phonon frequency dispersion, the linear-chain model has been used [40], which gives

$$\omega(q) = C' \sqrt{\frac{M_1 + M_2 + \sqrt{M_1^2 + M_2^2 + 2 M_1 M_2 Cos(qa)}}{M_1 M_2}} . \qquad (2)$$

For GaAs, a is the lattice constant, M_1 and M_2 are the atomic masses of Ga and As, respectively and C' is the fitting parameter. For semiconductor quantum dots (QDs), nanowires (NWs) or slabs, PCM is easily adapted using the appropriate expressions for the $d^3 q$ integration volume in equation (1).

Figure 8 shows calculated line shape of LO-phonon lines of GaAs by using the equation (1) and equation (2). The parameters used in equation (2) were M_1=69.723amu for Ga, M_2=74.922 amu for As and a=5.6533Å at 300 K for GaAs. The curves shown in Figure 8 were calculated for correlation lengths (L) of 30 nm, 20 nm, 10 nm, 5 nm and 3 nm. The value of Γ_0 was taken ~4.5cm^{-1} in the present case. Figure 8 shows that as the correlation length is decreasing (*i.e.*, confinement is increasing), LO line shape is more and more asymmetric along with shift towards low energy side. This clearly indicates that the downshift of the peak energy and asymmetrical broadening of the peak is mainly due to the contribution of the low energy phonons.
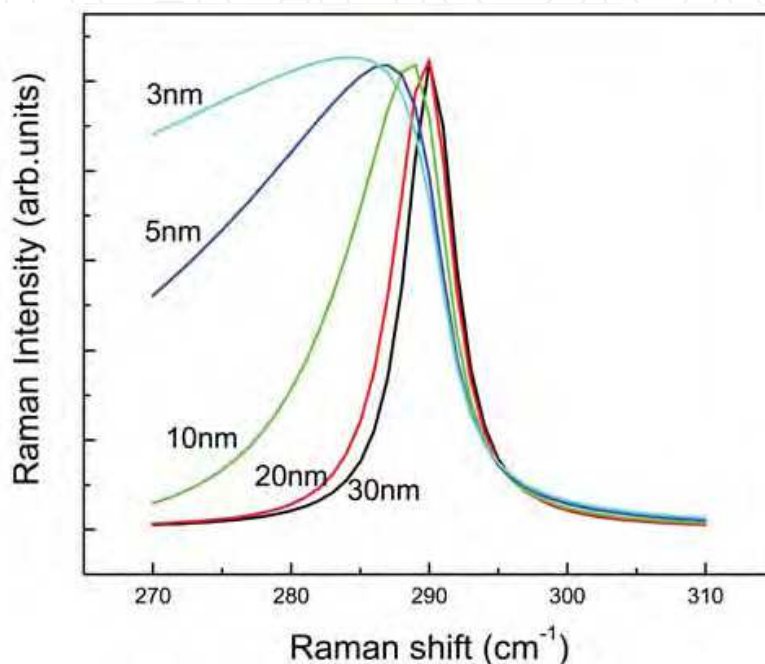

Fig. 8. Calculated Raman line shape of GaAs for different correlation lengths as calculated by using phonon confinement model [11] for GaAs. At 20nm and above 20nm the line shape is almost Lorentzian as the correlation length decreases below 20nm the line shape becomes asymmetric and downshifts

5.1 Defect density in GaAs and InAs NWs

Figures 9 (a) and (b) show the representative of the fitting of experimental LO phonon mode using equation 1 for the case of GaAs NWs (Figure 9 (a)) and InAs NWs (Figure 9 (b)). The fit shown in Figure 9 (a) gives the correlation length "$L=(10.00\pm0.41)nm$" in Mn-catalyzed GaAs NWs. The fit shown in Figure 9 (b) gives the correlation length "$L=(16.00\pm0.35)nm$" in Mn-catalyzed InAs NWs showing the good agreement of experimental data with theoretical curves.

The correlation lengths (L) obtained from LO fit for different samples of GaAs NWs were found in a range of 2 nm to 20 nm as summarized in Figure 10 (a) along with curves calculated by using equation 1. In our case, NWs lengths are as large as 20 µm while the diameters range from few tens to about 200 nm, therefore, by considering the nanowire length equal to 20 µm and the range of correlation length from 2 nm to 20 nm, defect (stacking faults) density would correspond to 0.5 to 0.05 defects/nm, respectively for GaAs NWs.
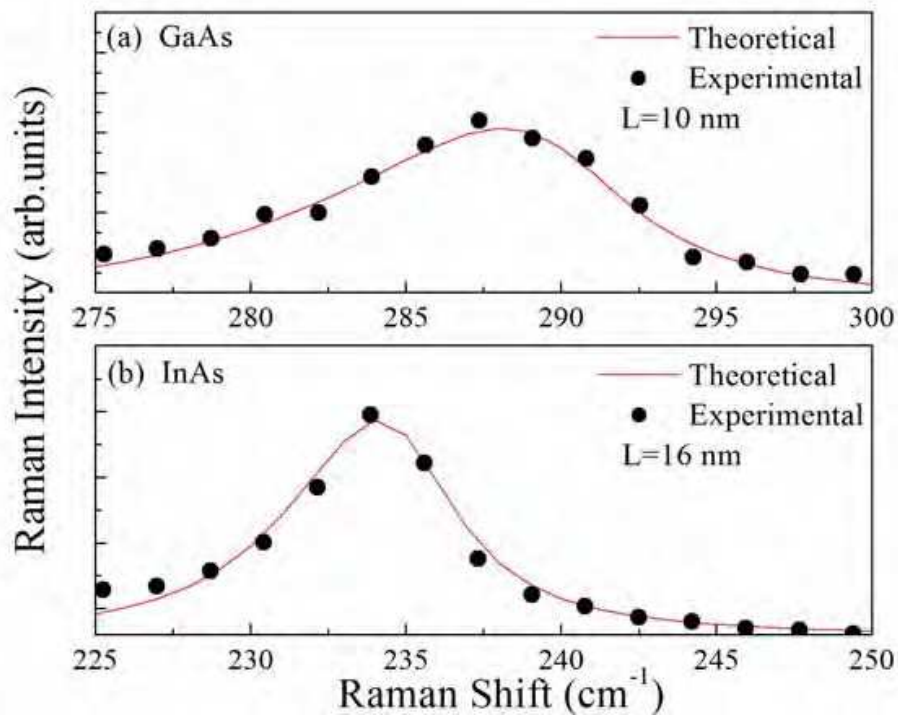
Fig. 9. Representative of the LO band in the Raman spectrum of Mn-catalyzed (a) GaAs NWs (b) InAs NWs along with the theoretical fitted curve by using the "phonon confinement model ". The correlation length (L) =10 nm for GaAs and 16 nm for InAs NWs.
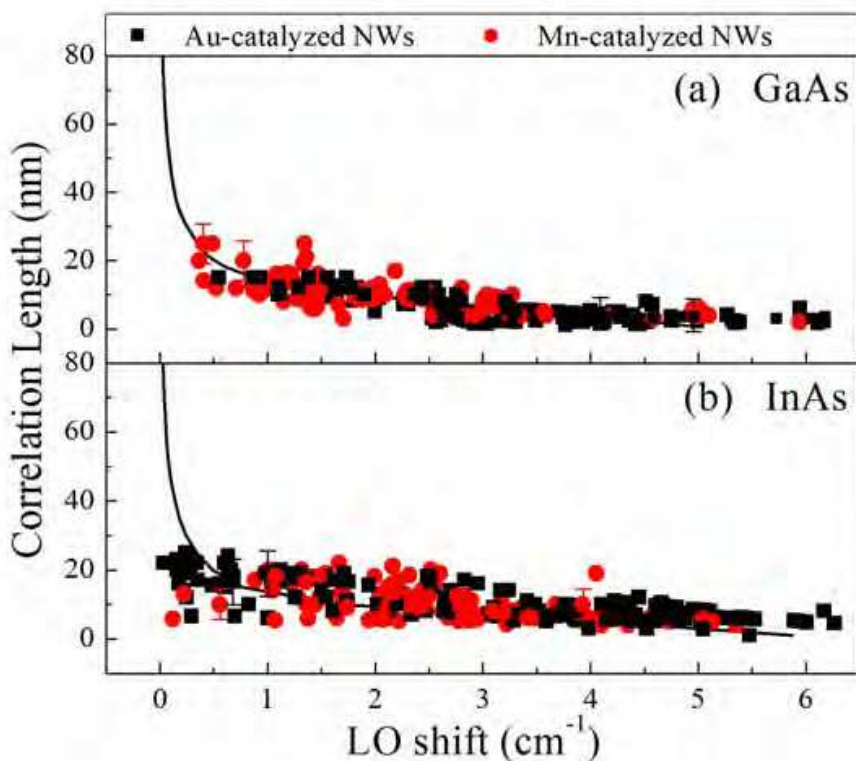

Fig. 10. Correlation length versus LO peak shift for Mn-catalyzed (dots) and Au-catalyzed (squares) (a) GaAs NWs & (b) InAs NWs in comparison of the theoretically calculated curve for GaAs and InAs bulk, respectively.

Figure 10 (b) shows the correlation length versus LO peak shift for Mn-catalyzed (dots) and Au-catalyzed (squares) InAs NWs in comparison of the theoretically calculated curve for InAs bulk. In case of InAs NWs correlation length was found to be in the range of $(1.0 \pm 0.8)nm$ to $(25.0 \pm 1.5)nm$ for Au-catalyzed and $(1.3 \pm 1.0)nm$ to $(22.0 \pm 0.8)nm$ for Mn-catalyzed NWs. Similar to GaAs NWs taking the InAs NW length equal to 20 μm and correlation length from 1 nm to 25 nm defect density (staking faults) corresponds to 1.00 to 0.04 defects/nm, respectively.

The fluctuations of the downshifts of the Raman line can then be understood to be due to variations in the defect density within the same growth batch or different batches, and in the same wire [18]. A similar explanation of the downshift of the Raman lines in Si NWs was given in the paper by Li and co-workers [41]. The smaller shift of the TO phonon is due to its smoother dispersion curve [42]. From the energy downshift the average dimension of the defect-free regions can be deduced.

6. Surface optical (SO) phonons

Surface optical (SO) phonons, activated due to vibrations confined to near-surface region, are observed in the compound semiconductors when the translational symmetry of the surface potential is broken. So far, SO phonon modes have been studied in thin films [43] and in micro-crystals [44], but not much literature is available on SO phonons in nanowire Gupta *et al.* [45] studied SO phonons in GaP nanowires. They clearly show that the SO phonon peak becomes more pronounced and downshifted with the increase of dielectric constant of surrounding medium. They also identified the symmetry breaking mechanism necessary for activating the SO mode with a diameter modulation along the wire, which arises from instability in the vapor-liquid-solid (VLS) growth mechanism. The dominant wavelength of this modulation was observed in TEM and found to be consistent with the theory for the band position.

Xiong et al. [46] studied the SO phonons in wurtzite ZnS nanowires. They studied the highly crystalline, rectangular cross-sectional W-ZnS nanowires grown by laser ablation. Similarly to the work of Gupta, they show that the downshift of the SO phonon frequency depends on the dielectric constant of surrounding medium. They also show that the dispersion of SO modes in wires with rectangular or circular cross section differs.

Spirkoska et al. [47] studied the effect of size and surrounding medium on the self catalytic GaAs NWs grown by MBE technique. They found that SO phonons are activated in the NWs with average diameter of 160 nm. By comparing the experimental data with that of theoretical curve they observe the larger shift in the SO phonon position especially for larger diameter. This larger shift was related to the hexagonal cross-section of the nanowires.

Above mentioned studies refer to the SO phonon mode activation due to the confinement along the diameter of the nanowires using the simple model based on electromagnetic theory proposed by Ruppin and Englman [49]. According to that model surface phonon frequencies in the cylinder can be calculated by the expression [49]:

$$\omega_{SO} = \omega_{TO} \sqrt{\frac{\varepsilon_o - \varepsilon_m \rho}{\varepsilon_\infty - \varepsilon_m \rho}} \; , \tag{3}$$

where ω_{SO} is surface phonon frequency; ω_{TO} is TO phonon frequency; ε_o, ε_∞ are static dielectric and dynamic dielectric constants, respectively; ε_m is dielectric constant of the surrounding medium and

$$\rho = \frac{[K_1(x)I_0(x)]}{[K_0(x)I_1(x)]} \qquad (4)$$

where I_n, K_n, are the modified Bessel functions and $x = qr$ (r being the radius of the NW). This model was successfully applied to describe the SO phonon spectra of microcrystalline spheres [44], GaAs NWs [47], Si NWs [48], and GaAs cylinders [50].

6.1 Surface optical phonons in GaAs and InAs NWs

There is another peak observed between LO and TO phonon peak marked by inverted solid triangle in the Figure 3 (a) & (b). We ascribe it as the surface optical phonon (SO). Inset shows the clear splitting of LO phonon mode and the SO phonon. Solid black lines in the inset are the experimentally recorded data while green lines are multiple peaks Lorentzian fit. This peak is not resolvable in all the cases. In case, this peak is not resolvable, LO peak shows more broadening and asymmetry probably due to weak contribution from the SO phonon. LO phonon lines were fitted with PCM to determine the correlation length, which also include SO phonon contribution.

SO modes are found to be activated in the cylinders with large surface to volume ratio and are simply related to the characteristic shape of the cylinder [47, 48, 50]. SO phonons are sensitive to the crystal defects and surface roughness. The position of the SO phonon modes depends on the dielectric constant of the medium that is surrounding the wires as well as on the diameter of the wires. In large crystals, phonons propagate to infinity and the 1st order Raman spectrum only consists of $q \approx 0$ phonon modes. When crystalline perfection is destroyed due to lattice disorder and defects, symmetry forbidden modes (like SO phonon modes) are activated and become stronger with increasing defect density.
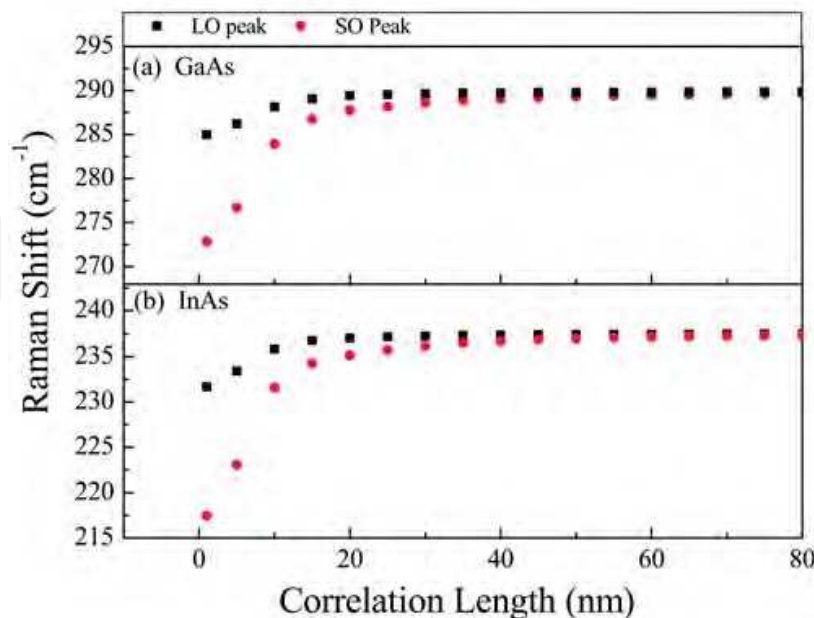

Fig. 11. Variation of LO and SO peaks of (a) GaAs and (b) InAs versus the correlation length as calculated by using the phonon confinement model (PCM).

SO phonons are activated when surface potential along the axis of the NW is perturbed by a strong component of wavevector q. Considering $q = 2k = 4\pi/\lambda_{ex}$ be the same as scattering vector in the back scattering geometry. Then for λ_{ex} = 514.5 nm corresponding value of q will be 0.0244 nm^{-1}. By using the peak position of SO phonons the corresponding diameter of NWs can easily be found from equations (3) and (4). If we take for GaAs NWs average value of $\omega_{SO(exp)}$ = 283.61 cm^{-1} then corresponding diameter of NW ($d = 2r = 2(x/q)$ calculated from equations (3) and (4) is ~45 nm, which lies in spread in the range of NWs diameter measured by SEM [7, 18, 26]. Similarly for InAs NWs with average $\omega_{SO(exp)}$ = 228.84 cm^{-1} it is found the corresponding diameter of NW ~88 nm.
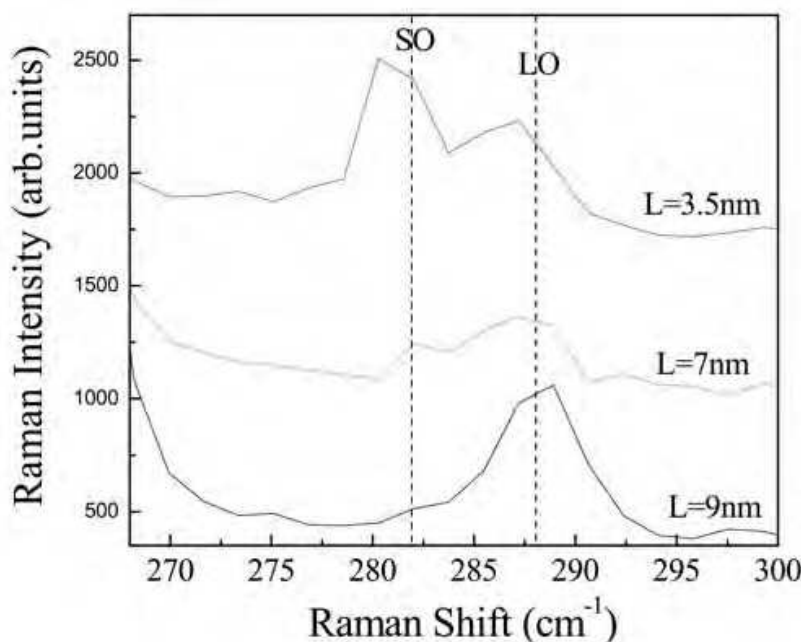

Fig. 12. Raman spectra of GaAs NWs for different correlation lengths showing that as the correlation length decreases, the SO phonon becomes stronger.

Many factors perturb the surface potential necessary for the SO phonon activation. This includes surface roughness of the NWs and the modulation of diameter along the growth direction during the VLS growth of the NWs [48]. During VLS growth the NWs grow continuously with the periodically modulated growth rate due to periodic change/modulation of available chemical species in the catalyst droplet. As a result of this modulation droplet will reshape periodically between nearly spherical and nearly ellipsoidal resulting in the formation of polytypic structure in the NWs and thus the stacking faults and twinning in the body of the NW [51]. Adu *et al.* [48] believe that the observation of SO modes should be a general indication of diameter modulation in the NWs.

In order to see the effect of defects (probably stacking faults in the present case) multiple curve fitting of the LO peak was carried out to determine the SO peak position. Correlation length corresponding to the curve containing both LO and SO elements was calculated by using the PCM. Figure 11 shows the behaviour of LO and SO phonons with correlation length for GaAs and InAs. The frequencies of SO phonon modes are found to be more sensitive to correlation length than LO phonon and for $L \leq 30$ nm, SO phonon energy can easily be separated from that of the LO phonon energy. When L varies from 10 nm to 1 nm
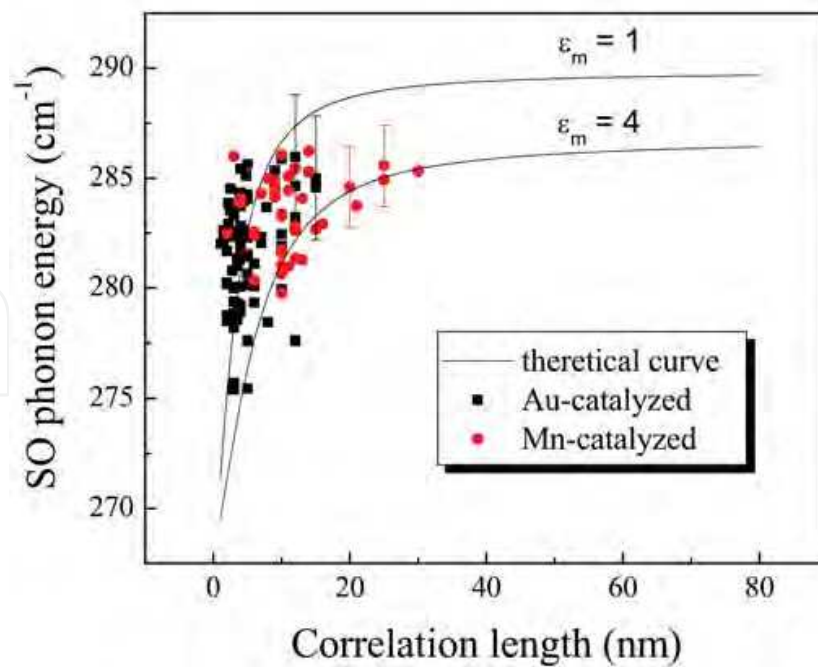
Fig. 13. Comparison of experimental and theoretical results for SO phonon vs correlation length. Solid line indicates the curve calculated by using the model presented by Ruppin et al [49] for two different values of the dielectric constant of the surrounding medium. Experimental data points for Mn-catalyzed GaAs NWs (dots) and Au-catalyzed GaAs NWs (squares) located on the theoretically calculated curve for the SO phonons in terms of correlation length
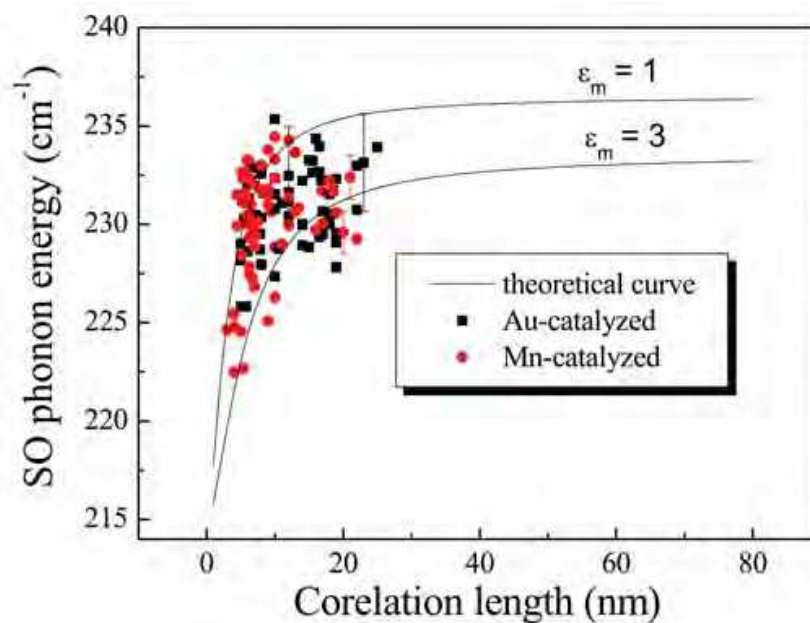

Fig. 14. Comparison of experimental and theoretical results for SO phonon vs correlation length. Solid line indicates the curve calculated by using the model presented by Ruppin *et al*. [49] for two different values of the dielectric constant of the surrounding medium. Experimental data points for Mn-catalyzed InAs NWs (dots) and Au-catalyzed InAs NWs (squares) located on the theoretically calculated curve for the SO phonons in terms of correlation length

SO phonon shows downshift of 11.1 cm^{-1}, while LO phonon shows downshift of only 3.2 cm^{-1} for GaAs. In case of InAs for variation of L from 10 nm to 1 nm, SO phonon shows downshift of 14.2 cm^{-1} and LO phonon shows downshift of 4.2 cm^{-1}. The energy separation between the LO and SO phonons of GaAs is found in the range of 0.10 cm^{-1} to 12.15 cm^{-1} (Figure 11) and 0.09 cm^{-1} to 14.22cm^{-1} for InAs, corresponding to correlation lengths of 100 nm to 1 nm. In case of NWs, where the energy separation was measurable, its value varies from (2.0 ± 0.4) cm^{-1} to (8.4 ± 0.3) cm^{-1} for GaAs NWs and (0.95 ± 0.51) *cm*$^{-1}$ to (8.79± 0.53) *cm*$^{-1}$ for InAs NWs, which lies in the calculated range. It also supports our argument that the peak located between the TO and the LO peaks can indeed be ascribed to Raman scattering from surface phonons.

Figure 12 shows the representative Raman spectra of the Au-catalyzed GaAs NWs indicating distinct appearance of SO phonons. The line shape analysis of these spectra gives correlation lengths of L = 9 *nm*, 7 *nm* and 3.5 *nm*. In Figure 12, it can be seen that for smaller correlation lengths the SO phonon peak is stronger than LO phonon peak and shifted downward in energy as was predicted by Ruppin *et al.* [49]. Figure 13 and 14 shows the experimental data points of GaAs NWs (Figure 13) and InAs NWs (Figure 14) for Mn-catalyzed NWs (dots) and Au-catalyzed NWs (squares) located on the theoretically calculated curves by using the equation (3) for the SO phonons as function of correlation length. In case of GaAs NWs maximum data of Au-catalyzed NWs shows good agreement for ε_m = 1, while for the case of Mn-catalyzed NWs, ε_m lies between 1 and 4. In case of InAs NWs, ε_m lies between 1 and 3 irrespective of the catalyst used. This variation of the dielectric constant can be justified by considering the oxide layer that surrounds the NWs.

As reported in Sec. 3, for the case of GaAs NWs, Au-catalyzed NWs have very thin oxide layer of only 1 nm thickness and Mn-catalyzed NWs have thick oxide layer of 4 nm [7, 18]. Similar to GaAs NWs thick oxide layer (2 nm to 3 nm) is surrounding the InAs NWs in both Au and Mn-catalyst [19]. This oxide layer consists of oxides of Ga, In and As, which have larger dielectric constant. This variation in the thickness of oxide layer may cause the variation in dielectric constant.

7. Conclusions

In this chapter, Raman characterization of GaAs and InAs NWs was carried out. GaAs and InAs NWs grown by MBE technique on different substrates at different temperatures by using Au and Mn as catalyst were characterized by Raman spectroscopy for their optical and structural quality. Raman spectra of GaAs and InAs NWs shows the downshift of LO and TO phonons along with asymmetrical broadening. This downshift and asymmetrical broadening of LO and TO phonons was related to the defects present in the body of the NWs. Variation in the downshift of LO and TO phonons was explained in terms of the defect density. Oxide related peaks on low energy side of the TO phonon were also observed in both Au and Mn-catalyzed GaAs NWs.

Phonon confinement model was used to calculate the average distance between the defects (*i.e.,* correlation length) and the defect density. Correlation lengths determined were (2.0 ± 0.1) nm to (15.0 ± 0.5) nm for Au-catalyzed and (2.0 ± 0.8) nm to (20.0 ± 1.5) nm for Mn-catalyzed GaAs NWs. In case of InAs NWs, correlation length was found to be in the range of (1.0 ± 0.8) *nm* to (25.0 ± 1.5) *nm* for Au-catalyzed and (1.3 ± 1.0) *nm* to (22.0 ± 0.8) *nm* for Mn-catalyzed NWs. The ccorrelation lengths in InAs and GaAs NWs were found comparable in both Au and Mn-catalyzed NWs.

SO phonons were also found to be activated in both types of NWs. In samples with shorter correlation length SO phonons are more pronounced and stronger as was predicted by

electromagnetic theory. An important conclusion drawn from the present study is that the structural quality of Mn-catalyzed NWs is comparable to that of Au-catalyzed wires, a feature that confirms Mn as an interesting alternative catalyst, especially in view of the possible fabrication of dilute ferromagnetic III-V based nanowires. Our results prove that Raman spectroscopy is a useful tool for rapid screening of the structural quality of semiconductor nanowires. This type of screening is important to give a picture of the real quality of the NWs growth.

8. Acknowledgements

9. References

[1] H. Ohno, H. Munekata, T. Penney, S. von Molnar and L.L Chang, Phys. Rev. Lett. 68 (1992) 2664.

[2] H. Ohno, A. Shen, F. Matsukura, A. Oiwa, A. Endo, S. Katsumoto and Y. Iye, Appl. Phys. Lett. 69 (1996) 363.

[3] G.A Prinz, Phys. Today 48 (1995) 58.

[4] Doo Suk Han and Jeunghee Park, Kung Won Rhie, Soonkyu Kim and Joonyeon Chang, Appl. Phys. Lett. 86 (2005) 032506.

[5] Y. Q. Chang, D. B. Wang, X. H. Luo, X. Y. Xu, X. H. Chen, L. Li, C. P. Chen, R. M. Wang, J. Xu, and D. P. Yu, Appl. Phys. Lett. 83 (2003) 4020.

[6] S. J May, J. G. Zheng, B. W Wessels, L. J Lauhon, Adv. Mater 17 (2005) 598.

[7] F. Martelli, S. Rubini, M. Piccin, G. Bais, F. Jabeen, S. De Franceschi, V. Grillo, E. Carlino, F. D'Acapito, F. Boscherini, S. Cabrini, M. Lazzarino, L. Businaro, F. Romanato and A. Franciosi, Nano Letters 6 (2006) 2130.

[8] W. S. Shi, Y. F. Zheng, N. Wang, C. S. Lee, and S. T. Lee, Appl. Phys. Lett. 78 (2001) 3304.

[9] B. Mandl, J. Stangl, T. Mårtensson, A. Mikkelsen, J. Eriksson, L. S. Karlsson, G. Bauer, L. Samuelson, and W. Seifert, Nano Lett. 6 (2006) 1817.

[10] A. L. Roest, M. A. Verheijen, O. Wunnicke, S. Serafin, H. Wondergem, and E. P. A. M. Bakkers, Nanotechnology 17 (2006) S271.

[11] H. Richter, Z.P. Wang, and L. Ley, Solid State Commun. 39 (1981) 625

[12] J. Chen, W. Z. Shen , J. B. Wang, H. Ogawa and Q. X. Guo, Journal of Crystal Growth, 262 (2004) 435-441

[13] Masahiro Kitajima, Critical Reviews in Solid State and Materials Sciences, 22 (1997) 275 – 349

[14] C. V. Raman and K. S. Krishnan, Nature, 121 (1928) 501

[15] G. Abstreiter, E. Bauser, A. Fischer, K. Ploog, Appl. Phys. Lett. 16 (1978) 345

[16] A.J. Pal, J. Mandal, Journal of Alloys and Compounds 216 (1994) 265-267

[17] J. B. Hopkins, L. A. Farrow and G. J. Fisanick, Appl. Phys. Lett. 44 (1984) 535

[18] S. Rubini, M. Piccin, G. Bais, F. Jabeen, F. Martelli and A. Franciosi, Journal of Physics: Conference Series 61 (2007) 992–996

[19] F. d'Acapito, M. Rovezzi, F. Boscherini, F. Jabeen, M. Piccin, L. Felisari, V. Grillo, G. Bais, S. Rubini, and F. Martelli, unpublished

[20] N Begum, M Piccin, F Jabeen , G Bais , S Rubini, and F Martelli, and A S Bhatti, J. Appl. Phys., 104 (2008) 104311

[21] N Begum, A S Bhatti, M Piccin, G Bais, F Jabeen, S Rubini, F Martelli and A Franciosi, Advanced Materials Research, 31 (2008) 23

[22] G. Burns, C, R. Wie, F. H. Dacol, G. D. Pettit, and J. M. Woodall, Appl. Phys. Lett. 51 (1987) 1919

[23] A. Mlayah, R. Carles, G. Landa, E. Bedel, C. Fontaine, and A. Munoz-Yague, J. Appl. Phys. 68 (1990) 4777

[24] G. D. Mahan, R. Gupta, Q. Xiong, C. K. Adu and P. C. Eklund, Phys. Rev. B 68 (2003) 073402

[25] H. Brugger, F. Schäffler and G. Abstreiter, Phys. Rev. Lett. 52 (1984) 142

[26] M. Piccin, G. Bais, V. Grillo, F. Jabeen, S. De Franceschi, E. Carlino, M. Lazzarino, F. Romanato, L. Businaro, S. Rubini, F. Martelli and A. Franciosi, Physica E 37 (2007) 134.

[27] T. R. Hart, R.L. Aggarwal, and B. Lax, Phys. Rev. B, 1(1970) 638-642

[28] G. E. Jelison, D. H. Lowndes and R. F. Wood, Phys. Rev. B 28 (1983) 3272

[29] G. D. Pazionis, H. Tang, I. P. Herman, IEEE J. Quantum Electron, QE-25 (1989) 976

[30] S. Piscanec, M. Cantoro, A.C. Ferrari, J.A. Zapien, Y. Lifshitz, S.T. Lee, S. Hofmann, and J. Robertson, Phys. Rev. B 68 (2003) 241312

[31] A. Freundlich, G. Neu, A. Leycuras, R. Carles, and C. Verie, In Hetroepitaxy on Silicon: Fundamentals, Structure and Devices, Material Research society Symposia Proc. 116 (1988)

[32] S. A. Lyon, R. J. Nemanich, N. M. Johnson, and D. K. Biegelson, Appl. Phys. Lett. 40 (1982) 316

[33] G. Landa, R. Carles, C. Fontaine, E. Bedel, and A. Muñoz-Yagüe, J. Appl. Phys. 66 (1989) 196

[34] I. H. Campbell and P. M. Fauchet, Solid State Commun. 58 (1986) 739

[35] K.K. Tiong, P.M. Amirtharaj, F.H. Pollak, and D.E. Aspnes, Appl. Phys. Lett. 44 (1984) 122

[36] P. Parayanthal and Fred H. Pollak, Phys. Rev. Lett. 52 (1984) 1822.

[37] A. Fischer, L. Anthony, and A. D. Compaan, Appl. Phys. Lett. 72 (1998) 2559

[38] R. L. Farrow, R. K. Chang, S. Mroczkowski, and F. H. Pollak, Appl. Phys. Lett. 31 (1977) 768.

[39] J. A. Cape, W. E. Tennant, and L. G. Hale, J. Vac. Sci. Technol. 14 (1977) 921.

[40] C. Kittle, Introduction to Solid state physics (Wiley, New York, 2003), 7th edn. Chapt. 4.

[41] Bibo Li, Dapeng Yu, and Shu-Lin Zhang, Phys. Rev. B 59 (1999) 1645.

[42] R. Shuker and R.W. Gammon, Phys. Rev. Lett. 25 (1970) 222 S.

[43] S. Ushioda, A.Aziza, J. B. Valdez, and G. Mattei, Phys. Rev. B 19 (1979) 4012.

[44] S. Hayashi and H. Kanamori, Phys. Rev. B 26 (1982) 7079.

[45] Rajeev Gupta, Q. Xiong, G. D. Mahan, and P. C. Eklund, Nano Lett., 3 (2003) 1745

[46] Qihua Xiong, Jinguo Wang, O. Reese, L. C. Lew Yan Voon, and P. C. Eklund, Nano Lett., 4 (2004) 1991

[47] D Spirkoska, G Abstreiter and A Fontcuberta i Morral, Nanotechnology 19 (2008) 435704

[48] K.W. Adu, Q. Xiong, H.R. Gutierrez, G. Chen, P.C. Eklund, Appl. Phys. A 85 (2006) 287–297

[49] R. Ruppin and R. Englman, Rep. Prog. Phys. 33 (1970) 149

[50] M Watt, C M Sotomayor Torres, H E G Arnot and S P Beaumont, Semicond. Sci. Technol. 5 (1990) 285

[51] Yufeng Hao, Guowen Meng, Zhong Lin Wang, Changhui Ye, and Lide Zhang, Nano. Lett. 6 (2006) 1650.

Nanowires

Edited by Paola Prete

ISBN 978-953-7619-79-4

Hard cover, 414 pages

Publisher InTech

Published online 01, February, 2010

Published in print edition February, 2010

This volume is intended to orient the reader in the fast developing field of semiconductor nanowires, by providing a series of self-contained monographs focusing on various nanowire-related topics. Each monograph serves as a short review of previous results in the literature and description of methods used in the field, as well as a summary of the authors recent achievements on the subject. Each report provides a brief sketch of the historical background behind, the physical and/or chemical principles underlying a specific nanowire fabrication/characterization technique, or the experimental/theoretical methods used to study a given nanowire property or device. Despite the diverse topics covered, the volume does appear as a unit. The writing is generally clear and precise, and the numerous illustrations provide an easier understanding of the phenomena described. The volume contains 20 Chapters covering altogether many (although not all) semiconductors of technological interest, starting with the IV-IV group compounds (SiC and SiGe), carrying on with the binary and ternary compounds of the III-V (GaAs, AlGaAs, GaSb, InAs, GaP, InP, and GaN) and II-VI (HgTe, HgCdTe) families, the metal oxides (CuO, ZnO, ZnCoO, tungsten oxide, and $PbTiO_3$), and finishing with Bi (a semimetal).

INTECH

open science | open minds